Meas. Sci. Technol. 1 (1990) 107–119. Printed in the UK

Sub-nanometre displacements calibration using x-ray interferometry

D K Bowen, D G Chetwynd and D R Schwarzenberger

Centre for Microengineering and Metrology, Department of Engineering, University of Warwick, Coventry CV4 7AL, UK

Received 19 December 1988, in final form 27 July 1989, accepted for publication 15 August 1989

Abstract. The technology of x-ray interferometry has been applied to the calibration of micro displacement transducers at sub-nanometre levels. Using the lattice spacing of high perfection silicon of semiconductor industry grade as a reference, the system provides a portable, absolute length standard with an accuracy of 1 part in 10^6 traceable to primary standards, a demonstrated resolution of 10 picometres and a double-beam phase-quadrature output for providing sensitivity to the direction of motion of the moving interferometer blade. The system and its performance are discussed in detail, methodologies for the analysis of data are presented and an application to the calibration of Talystep transducers (both absolute and comparative between models) for overall accuracy and thermal drift is reported. The design and performance of a portable instrument using a miniature x-ray source is also reported.

1. Introduction

'Nanotechnology' is an emerging discipline with applications and implications in many areas of science and engineering, including the fabrication of microelectronic circuits, the manufacture of optical recording and data retrieval machines, the manufacture of mirrors for x-ray astronomy and the direct manipulation of DNA in genetic engineering. The ability to perform manipulation and to control manufacturing at precisions ranging from 100 nm down to sub-nm levels rests ultimately upon the availability of reliable, traceable metrological techniques in this region. A surprising number of techniques do in fact have sensitivity to displacements of the order of a nanometre, including fringe-division optical interferometry, optical slope-deflection integration, differential transformer transducers such as the Talystep, capacitance probes, the scanning tunnelling microscope and the atom force microscope. These rely upon several different physical principles delimiting the interaction of the probe with the specimen or component. The stylus methods depend upon physical contact, in which the indentation of the specimen under stress must be evaluated. Optical methods depend upon the optical properties of the surface and, for example, the reflectivity of a metal is a function of the electronic conditions in the top 20 nm or so of the material and is not rigorously isolated at the surface atomic layer. Capacitance methods depend upon the charge distribution near the surface of the material, and are strongly influenced by its conductivity. Scanning tunnelling methods, which hold enormous promise for the achievement of high lateral as well as normal displacement resolution, rely upon the quantum physics of the interaction between the specimen and the probe, and can be strongly influenced by surface conditions unrelated to surface topology. The atom force microscope essentially measures van der Waals forces between the specimen and a probe as a function of lateral position. In all of these methods (and, one suspects, in any conceivable method that has nanometre sensitivity) there are circumstances or specimens for which it is not at all clear what is being measured, let alone what is the precision of the measurement. Calibration methods in the nanometre range are thus absolutely essential.

Existing step standards for calibration of such instruments are produced by evaporation, etching or plating and are traceable to optical wavelengths. However, it has not as yet been possible to produce satisfactorily calibrated standards for steps below about 25 nm, and it may not be assumed that the massive extrapolation required from existing calibration standards down to atomic dimensions is justified. This paper reports the establishment of x-ray interferometry as a methodology for the calibration of engineering transducers in the range 10 pm–100 nm.

The method of x-ray interferometry relies upon the availability of highly perfect, homogeneous single crystals, of any convenient material, available in reasonably large sizes (comparable with engineering transducers). An instrument can be made out of such crystals that, in combination with an x-ray source, can be used to produce sinusoidal variations of x-ray intensity in the detector, with identically the same translation period as that of the crystal lattice itself. If x-ray interferometers

0957-0233/90/020107 + 13 $03·50 © 1990 IOP Publishing Ltd

and mechanical transducers can be operated simultaneously to measure the same displacement, a reproducible calibration system is thereby achieved. If the lattice parameter of the crystal can be determined in absolute units, a portable length standard is also achieved. If crystals from different sources are highly similar then an internationally achievable length standard is automatically achieved. Crystals of silicon manufactured for modern semiconductor electronics fulfil all of these requirements. The attainment of a portable length standard without further calibration reduces, essentially, to the specification of a maximum impurity level and an impurity description. Semiconductor silicon crystals are normally homogeneous and reproducible, one with another, to a few parts in 10^6. Selected crystals are homogeneous to better than one part in 10^7, and x-ray methods exist to compare the lattice parameter of one crystal with another to 2 or 3 parts in 10^8. The correlation of the silicon lattice spacing to absolute standards has been performed at the National Bureau of Standards (NBS) (USA) and the Physikalisch-Technische Bundesanstalt (PTB) (FRG) to a precision of about 1 in 10^6.

X-ray interferometry was invented by Bonse and Hart (1965) and its potential application to metrology was soon realised in a paper by Hart (1968) entitled 'An Angstrom Ruler'. The referencing of the silicon lattice spacing to optical wavelength standards was first performed by Deslattes and Henins (1973) using the NBS krypton standard and the measurements have since been refined at the PTB (Becker *et al* 1982). The demonstration that an x-ray interferometer could be operated simultaneously with a mechanical engineering transducer (a Rank Taylor Hobson Talystep) with a stylus in contact with the moving part of the interferometer was performed by Chetwynd *et al* (1983) using an interferometer loaned by Hart. They showed conclusively that simultaneous operation was indeed possible without undue interference from mechanical vibration coupling, and that controlled movements around a nanometre could be measured simultaneously on both instruments. A major research project was then sponsored by the National Physical Laboratory and preliminary results have been reported by Bowen *et al* (1985) and by Whitehouse *et al* (1988). A large, very high performance x-ray optical test bed and a convenient portable instrument, both containing some innovative features, have been designed, constructed and evaluated in detail. This paper presents the design principles of the systems, describes their construction and performance, discusses the data analysis and the limitations of performance, and describes the application of one of the instruments to the absolute and comparative calibration of Talystep transducer heads together with an assessment of their thermal performance.

Talystep transducers are linear differential inductor half-bridges of exceptional sensitivity. Although these are theoretically capable of infinitesimal resolution it is not known whether a particular implementation may have small-scale structure and in any case mechanical and electrical noise will restrict the discrimination achievable in practice. Whitehouse *et al* (1988) examine this last point in some detail and, by using a rather conservative model, estimate the achievable noise level for a Talystep as certainly below 0.2 nm. Results from Franks (1984), Bowen *et al* (1985) and Chetwynd (1987) all show rather better performance being achieved in practice. Bowen *et al* conclude that, given a moderate amount of data analysis, a discrimination of 10 pm is obtainable with a Talystep transducer.

It seems that improvements in transduction are likely to be only marginal and the arguments used for evaluating inductive transducers have their equivalents for, for example, capacitive ones. Thus a calibration system sensitive to better than 20 pm should be satisfactory and that figure is used as the target specification for the work reported here.

2. X-ray interferometer instrumentation

2.1. The x-ray interferometer

When a perfect crystal is illuminated by a monochromatic x-ray beam at the Bragg angle there are three emergent beams (figure 1) as predicted by the dynamical theory of x-rays. The attenuated incident beam is of no interest here except as a source of background noise. The diffracted and forward diffracted beams emerge symmetrically if a suitable geometry is adopted, as illustrated, and both 'know' the spatial phase of the lattice which they have traversed. The x-ray interferometer exploits this beam-splitting property as shown in figure 2. It is machined from a single crystal block to give three parallel blades, the third of which can be moved in its own plane relative to the other two. An x-ray beam

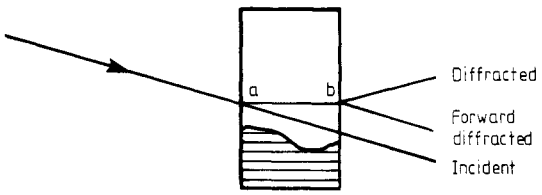

Figure 1. Dynamical diffraction of x-rays through a perfect crystal.

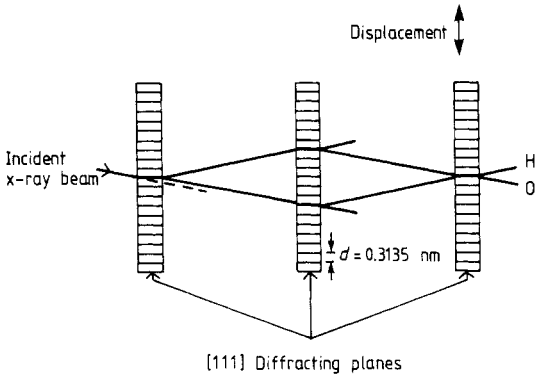

Figure 2. X-ray optics of the interferometer.

incident at the correct Bragg angle is diffracted by the first blade and again by the second; those beams recombining at the third blade are diffracted with intensities dependent on the position of the phase maxima in the combined wavefield relative to the atoms in the crystal lattice. Then, as the third blade is translated, the output intensity varies sinusoidally with the periodicity of the diffracting planes. It is important to note that this periodicity depends only upon the spacing of the diffracting planes and not the x-ray wavelength. Operation is also possible by traversing the middle blade relative to the outer ones.

For ideal 'thin crystal' blades the diffracted and forward diffracted beams are expected to be out of phase by 180°, but will be in phase for thick blades with 'anomalous' transmission. In any intermediate case some phase difference may be expected. The sinusoidal variation of the diffracted beam (H) has much lower contrast from background noise than that of the forward diffracted beam (O).

Hart's designs for realising a practical device were based on a monolithic construction, with the blades and an elastic traverse mechanism machined from a single crystal of high-grade silicon, with the blades about 4 mm × 2 mm × 0.5 mm thick and spaced 2–3 mm apart. Separated blade interferometers have also been built (see, for example, Becker *et al* 1982). Usually the blades are oriented to give diffraction by the [220] planes, yielding an output periodicity of 0.192 nm.

The principles embodied in the monolithic design are ideal for metrological work, but the detailed construction is unsuitable for a transducer calibrator because it is not possible to separate out the force loop that deflects the blade from the metrological loop which references the transducer to the monolith. Chetwynd *et al* (1983) proposed a new design in which a larger monolith is used as a metrological reference. The interferometer used in this work follows that design, but because of the capacity of machines available for its manufacture it is somewhat smaller (figure 3). It is manufactured from float-zone silicon. The blades are approximately 5 mm × 10 mm × 1 mm and are spaced about 15 mm apart. The block, excluding blades, is 42 × 30 × 22 mm and has grooves

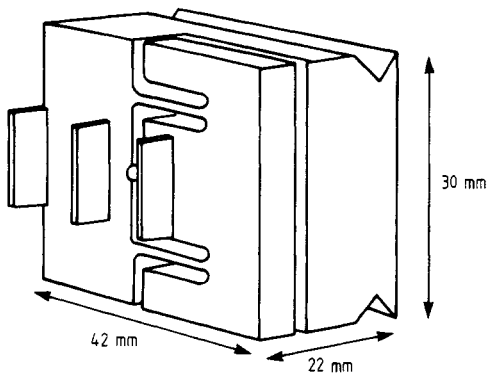

Figure 3. Dimensions of the interferometer. The complete device is cut out of a monolithic block of silicon single crystal.

machined along its top and bottom surfaces to provide kinematic locations. The traverse of the third blade is effected by isolating a 5 mm thick section of the block except for two thin strips, about 20 mm long, which form an elastic mechanism equivalent to a symmetrical four-bar chain (see, for example, Smith *et al* 1987). Deflection is caused by a magnet and solenoid force transducer (Smith *et al* 1987), the magnet being glued to the bottom surface of the interferometer. The probe of the displacement transducer that is to be calibrated rests against the top surface of the moving element. Both magnet and probe are in line with the blade, which is located centrally between the springs in order to minimise parasitic deflections. The cantilevered sections and slitting ensure that there is a long path from the point of application of any load to the blade and so, by St Venant's principle, the strain in the blade will be minimal. The combination of spring stiffness and coil design used gives a nominal deflection sensitivity of the order of 1 nm mA^{-1} or 4 nm V^{-1}. The use of [111] planes for diffraction gives a periodicity of 0.313 562 5 ± 0.000 001 6 nm at 20 °C. The instrumentation advantage in the greater intensity diffracted by these planes outweighs any decrease in sensitivity from the greater periodicity compared with the use of [220] planes.

The manufacture of the monolith, by Professor M Hart, was by diamond sawing and high-speed diamond milling, followed by etching to remove subsurface damage. The design sizes are not critical; the size and spacing of the blades is governed by the requirement that the relevant beams are incident within the blade area and thus by the Bragg angle for the longest wavelength likely to be used (copper K_α). Size is also governed by the space required for beam-stops and the need to minimise the effects of any lattice spacing variation by using a small area. Tolerance on blade spacing is not critical, it being necessary only that the recombining beams meet within the third blade. Neither is the centralisation of the blade on the springs critical as the stiffness of the system in directions other than that of traverse is very high. Errors in the machining of the springs will alter their stiffness, but this can be calibrated out in use. Any asymmetries may produce parasitic deviations but these should be negligible over the deflection used in the system. Tolerances of several tens of micrometres are quite acceptable. The effect of misorientation between the lattice and the traverse direction depends on the cosine of the angular error and so is readily controlled to acceptable limits. The surface figuring and finish of the blades is rather more critical as they affect the output contrast, see § 2.4. In practice a compromise is reached between manufacturing convenience and fringe contrast with the straightness and parallelism of the blades being controlled to a few micrometres over their active area.

2.2. The x-ray optical test system

The evaluation of the x-ray interferometer-based calibrator required the development of two major systems: a metrological system for referencing the trans-

ducer to the interferometer, controlling traverses and monitoring outputs and an x-ray optical test-bed of good mechanical and thermal stability on which to operate it.

The mechanical design and performance of much of this work is published elsewhere, by Bowen *et al* (1985) and Chetwynd (1987) on the test-bed and by Whitehouse *et al* (1988) on the metrological mounts. Only a brief overview will be given here. The test-bed is quite large to allow flexibility of application. It uses a sand-filled horizontal, extruded aluminium optical bench on which various devices can be mounted relative to an x-ray source mounted on a horizontal axis radius arm. Both of these are mounted onto a cast iron bed which then rests on a concrete block 2.5 × 0.5 × 0.5 m in size. This stands on the floor of a basement room through an active, servo-levelling air-spring suspension. Thermal, radiation and acoustic shielding is achieved by enclosing all of this within a cabinet of plywood/lead sandwich. The x-ray tube is a water-cooled, fixed anode type driven from a generator of 60 kV, 60 mA capability. Silver, molybdenum and copper anode tubes are available on the system. The actual maximum power available depends upon the tube and is typically 1500 W.

The reasoning behind the design of monolithic interferometer proposed by Chetwynd *et al* (1983) was that its top and bottom surfaces should act as metrological bases. Particularly, the transducer that is to be calibrated, mounted in a suitable frame, would rest kinematically on top of the monolith held in place by its weight (a body force being the ideal for kinematic force closure). However, the small platform area of the monolith actually produced was insufficient to allow the stable mounting of a transducer as large as the Talystep by this means. Thus a considerably more complex mechanical system had to be used with, inevitably, some degradation of the system performance from its ultimate potential. Figure 4 shows the essential features. All active components are referred to a central block, the lower ones pushed up, against gravity, by springs. The upper parts are also pulled upwards by springs against a hard friction clamp. This allows easy adjustment of the Talystep position during set-up. The use of thin sections under tension in the clamp takes out the residual misalignments of the non-kinematic construction in a manner akin to a universal joint. The whole design separates out, as far as is possible, the metrological and force loops of the system. Particular care is taken to avoid bending stresses in the reference plate.

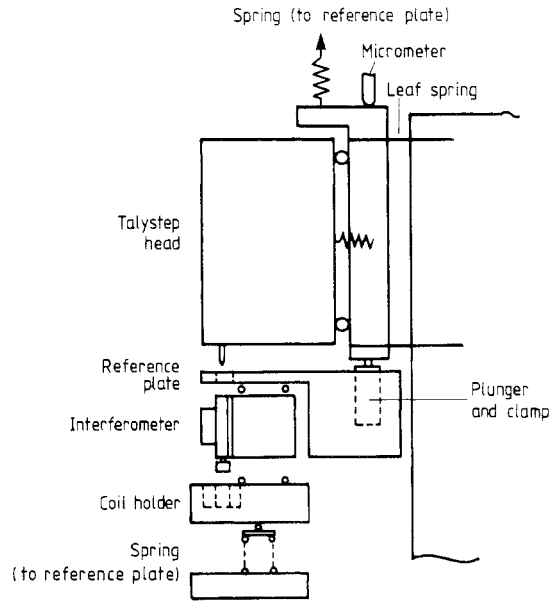

Figure 4. Details of the interferometer mount.

The input beam to the interferometer is taken off from the x-ray source at the conventional 6° angle and a brass collimator about 150 mm long limits the beam to a rectangle 1 mm high by 3 mm wide at the first blade. The desired output beam is selected by a slit, 10 mm × 2 mm in cross section and 50 mm long, through a brass block and is measured by a Nuclear Enterprises scintillation detector capable of count rates of up to 50 k CPS (counts per second). Both the Bragg angle adjustment of the source and the angle and position of the slit are remotely controlled from outside the enclosure. The instrumentation is controlled by either an Olivetti M24 or a BBC (model B with extended memory) microcomputer, the latter being perfectly adequate for logging to disc, supplying a colour display of the measurement in real time and performing simple analysis of the data. An IEEE 488 interface communicates with a 'Minicam' system (Rodriguez and Siddons 1979) supplied by Bede Scientific Instruments, which contains analogue-to-digital (ADC) and digital-to-analogue (DAC) converters and scaler modules. The DAC supplying the drive to the displacement coil is a low-cost 12-bit single chip device boosted for current drive capability by a very simple 355-based amplifier. With the spring stiffnesses and coil used in the prototype, one bit corresponds to a displacement of approximately 13 pm. A current limit of 20 mA ensures that there can never be a large thermal input but restricts the range on this system to 20 nm although the interferometer itself is capable of a much larger range. The Talystep amplifier output is logged by a 13-bit, 20 ms conversion-time ADC giving a resolution of about 2.5 pm at an amplifier magnification setting of 10^6 and 10 pm at the 200 000 gain used for most of the results published here. The scalers are most commonly operated over counting periods of 1 or 5 s. Under typical operating conditions an average count rate is around 2000 CPS which gives, assuming a Poisson distribution, a 99.7% confidence interval of ±134 CPS (7%) for a measurement over 1 s and ±60 CPS (3%) for one over 5 s. The Talystep signal accuracy is ±5% due to amplifier, converter and calibration uncertainties. In addition, mechanical and electrical noise at the input contributes a random fluctuation of the order of 20 pm RMS at 2 Hz bandwidth.

The mechanical stability of the system is extremely good. Vibration isolation of a high degree is indicated by the low noise figures quoted above. Basic static stability over a period of weeks is sufficiently high to be undetectable within the variations caused by thermal expansion. The temperature sensitivity is discussed in § 4.

The overall performance is demonstrated by figure 5,

which shows the response of the Talystep and the x-ray intensity to a coil drive signal corresponding to a nominally triangular wave of 1 nm amplitude stepped in increments of 13 pm. The counting interval was 5 s for each point. The computer output linearly interpolates between points. As there are approximately 3.2 lattice spacings in 1 nm, the fidelity of the drive system is well highlighted. The results of many tests, not readily reproducible here, show that the Talystep signal follows closely the displacement demand and that the transducer is able to respond accurately to very small signals, even though there will be a superimposed thermal drift. Note the well defined reversal in the fringe pattern which occurs at the reversal of the demand signal. The electromechanical transducer driving the third blade responds well at the 10 pm level, as does the Talystep which also displays a distinct reversal.

2.3. Double-beam x-ray interferometry

Chetwynd *et al* (1983), building on ideas of Hart (1968), proposed that phase quadrature output beams be developed for the x-ray interferometer so that the direction of traverse of the third blade could be directly monitored, to make a super-precision incremental displacement transducer. They suggested that two source beams, one passing through a quarter-wave plate, be incident on the interferometer with two miniaturised scintillation detectors monitoring the output. Two other possibilities may be considered.

The two output beams of the interferometer (O and H in figure 2) may have a phase difference between them and this was investigated using both molybdenum and silver x-radiation. Simultaneous fringes on both beams were readily detected but with a relative phase of about 170° for Ag K_α and 90° for Mo K_α rather than 180° as expected for the ideal 'thin' blades. A near quadrature condition was directly available with the particular monolith used. However, it was shown that non-uniformity of the blade thickness was sufficient to influence the phase relationship even with the more penetrating silver radiation and, of course, the actual phase obtained depends on the blade thickness actually produced. Phase corrector plates could be applied if the blade uniformity is sufficiently good, but, given the inherently poorer contrast of the diffracted (H) beam, this method is not attractive. If fine trimming of the blades, including selective thinning to produce an in-built quarter-wave plate becomes practical, for example by ion-beam machining, this decision could be reviewed.

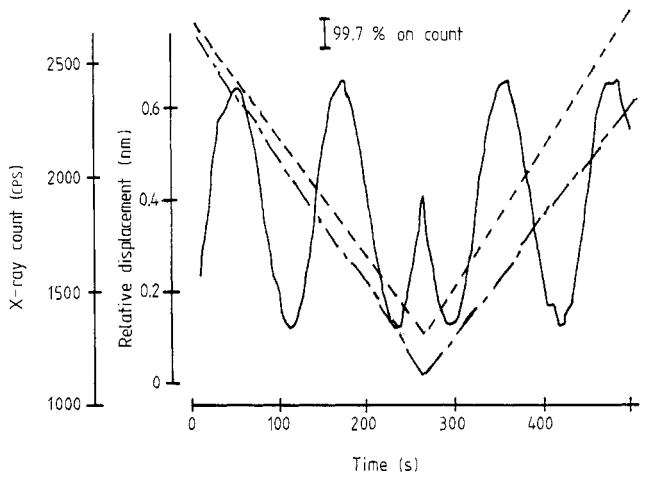

Figure 5. Performance of the interferometer with traces of the coil demand signal and of the Talystep output. Note the 'mirror' reversal of the fringes when the direction of travel is reversed. ---- Coil demand; ——— Talystep output; —— x-ray intensity.

Another approach is rather closer to the original proposal: part of one reasonably large source is phase accelerated† by a phase plate and a movable slit used to chop the output signal so that either the accelerated or normal part is detected. This is a low-cost solution, requiring only one detector but it has the following disadvantages. A mechanical movement is introduced into a highly sensitive system and it is difficult to avoid exciting vibrations while switching at reasonable speeds. Also, counting of the two signals takes place sequentially, so the response speed of the system is at least halved. This conflicts with the desirability of minimising total measurement time in systems of such high sensitivity. Nevertheless, a successful system of this type has been designed and tested. Referring to figure 2, a phase plate is introduced across half the width (into the page) of the lower beam between the second and third blades. A small, 1 mm thick tantalum flag, with edges well defined by grinding, is placed in the exit beam ahead of the detector slit. This is switched between two stable positions by a small solenoid activated by a logic signal from the instrumentation computer so as to allow transmission of either half of the beam to the counter. The phase plate consists of a small piece of high quality Kapton film, 100 μm thick, trapped between thin metal plates such that a square of about 2 mm side protrudes. It is supported on an adjustable kinematic location from a bracket attached to the interferometer reference plate (see figure 4) and its position adjusted so that the phase of the outer half-beam only is altered. The phase difference between the two half-beams may be adjusted by rotation of the Kapton about a horizontal axis. With 100 μm nominal thickness, rotation through 16° from the vertical increases the path length by 4 μm, giving a phase lead of 90° with Mo K_α radiation.

As less than half the beam power in the single beam interferometer is available to each channel, counting times on each must be doubled to get the same confidence levels in the fringes, implying an increase by a factor of four in the time for a complete measurement cycle (although it will have increased information content). In practice, as the fringe division requirements are not great, rather poorer statistics may be acceptable in order to obtain rather higher operational speeds. On the prototype system, better contrast is obtained from each half of the chopped beam than from the diffracted (H) beam. Using molybdenum K_α radiation, results such as

† The refractive index of x-rays is <1 so their phase velocity is higher in denser media.

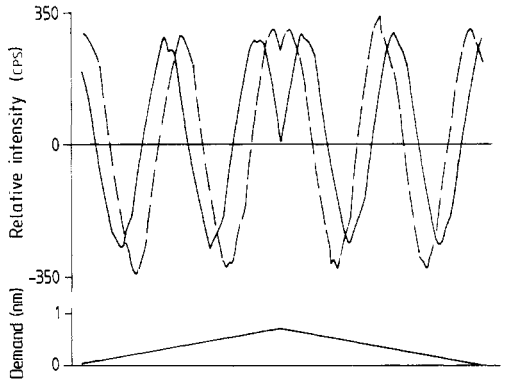

Figure 6. Two-beam interferometry using a chopper and phase plate. Again a reversal is shown. Total duration of signal is about 1000 s.

figure 6 are produced with the chopped beam system. The figure shows the count rate for both counter channels and the coil demand signal, a nominal 0.6 nm amplitude triangular signal. The Talystep signal has been suppressed for clarity. The counting time for the scalers is 5 s. Comparing the fringe quality with that in figure 5, it is seen that a very acceptable performance can be obtained with little penalty in operational time. The chopped beam system has proved to be highly practical.

2.4. Fringe contrast

During manufacture of the interferometer, the silicon crystal is sawn and then etched isotropically to remove surface damage; the thicknesses of the blades are thus not completely uniform, so that the path length and hence the phase may vary across the blade. If the incident x-ray beam is wide, the intensity and phase from different areas will be integrated, giving a decrease in contrast of the fringes. Although partial cancellation reduces contrast, phase variation does not otherwise affect fringe interpolation. The fringes here are intrinsically sinusoidal, unlike the optical case, and so no harmonic distortion is introduced. For Mo K_α radiation diffracted by Si(111) planes, 22 μm extra path length produces a phase shift of 180° (Hart 1975).

If beam intensity is shared equally between two parts having a phase difference, φ, the peak amplitude will be reduced by a factor $\cos(\varphi/2)$ compared with the ideal. If the intensity is spread uniformly across a band of phases of width φ, the reduction is $(2/\varphi)\sin(\varphi/2)$, a less serious degradation. A path difference of about 15 μm as a step or 26 μm of silicon spread uniformly would reduce the intensity by 0.5. As the beam area is reduced the fringe contrast may be expected to increase, but then the total number of x-ray counts is reduced and again a compromise is reached experimentally.

The contrast obtained with the present interferometer is very variable, some areas giving little fringe contrast and others up to 0.3, where contrast is defined as amplitude/mean on the forward diffracted beam. Profiles taken by a Talysurf across one surface of the blade of a similar interferometer showed variations in depth of about 7 μm, so that with a total of six surfaces for the beams to pass through, the contrast variation is not surprising. For desirably high contrast, manufacturing tolerances need to be nearer 1 μm.

Also, during manufacture, small internal strains may be created so that the moving blade may be slightly twisted relative to the other two, and this leads to reduced fringe contrast. The twist may be estimated by measurements of the spatial moiré fringes on a film placed in front of the slit and counter. For the present interferometer the intrinsic twist is of the order of 0.03 seconds of arc, the moiré fringe spacing about 2 mm. This may be corrected by applying a compensating couple using small weights on a lever arm glued to the moving section of the interferometer. If the twist is 0.15 seconds of arc the contrast is halved, and no intensity fringes are detectable if it becomes as great as 0.2 seconds.

The contrast is also affected by background noise from scattering after the required beam has traversed the interferometer. Thus the slit needs to be carefully aligned, and made of a material that does not fluoresce with the radiation used, and any scattering from the direct x-ray beam must be prevented from entering the detector.

When directional information is required so that two beams in phase quadrature are to be detected, then the contrast may be reduced as well as the average intensity. If the diffracted (H) beam is used, its contrast is much less than that of the forward diffracted (O) beam, the fringes more jagged, and any analysis correspondingly less accurate. If the forward diffracted beam is divided, the beam nearer the body of the interferometer more often gives lower contrast but a higher intensity than that nearer the edge of the blade. This follows from the way the blades are sawn during manufacture. Any variation in path length introduced by irregularities in the phase plate will, however, affect only the beam nearer the edge of the blades in the present arrangement, so the two sets of fringes have fairly similar contrast.

3. Data analysis

Techniques for optical fringe division are well known (see, for example, Creath (1988) for a recent review) and it is to be expected that similar methods will apply to x-ray interferometry. While this is broadly the case, the different detection conditions impose different uncertainties onto the fringe data so that it is not obvious that the rules for optical fringes apply exactly to the present situation. The physics of the x-ray interferometer ensures that the fringes are inherently sinusoidal with blade displacement. However, the contrast is generally poor compared with typical optical interferometers. The low x-ray intensity and the use of photon-counting detectors means that the fringe signal is noisy but the noise is known to be Poisson distributed and can be evaluated directly. The detector is inherently linear so that fringe sinusoidality is preserved. In contrast, optical detectors have non-linearity and are subject to electronic noise which is not quantifiable from the signal. These differ-

ences render unsafe the assumption that information on the accuracy of optical fringe division can be applied directly to x-ray fringes. As our purpose is to establish the metrological bounds which analysis places on x-ray interferometry it is necessary to undertake a full study of the fringe division process. This is given below in some detail so that the context and exact nature of assumptions and approximations in the derivations are clearly shown.

Optical fringe division is virtually always undertaken using a multiphase method and similar methods can be directly applied to x-ray interferometry (Schwarzenberger *et al* 1989). However, unlike the optical case, measurement times are of the order of seconds for each point on the fringe and, in the system being considered, that time rises directly with the number of phases. For many measurements there is a practical incentive to use a single-phase system. All standard interpolation methods are based essentially on the least-squares fitting of sinusoids to the fringes. With the lower information content of a single-phase system and with uncertain contrast in the fringe it is no longer clear that such algorithms perform more accurately than simpler approximations. Methods based on Stirling approximations perform adequately and, being simpler, have better reliability and faster execution. Hence the discussion below is centred on this approach.

3.1. Measurement of a displacement

For a displacement imposed by the magnet and coil, the nominal distance is given by the coil voltage after prior calibration using fringes; this is then refined by analysis of the fringes.

The Stirling approximation is used to give the intensity J_m of a fringe maximum or minimum from the measured intensity at three equidistant sampling points centred approximately on the extreme value.

$$J_m = J_2 - \frac{(J_1 - J_3)^2}{8(J_1 + J_3 - 2J_2)}. \tag{1}$$

Then the 'zero crossing' intensity (DC level), Z, and fringe amplitude, A, follow from $\frac{1}{2}(J_{max} \pm J_{min})$. An unknown displacement is measured by counting the number of fringes between zero crossings, and adding end fractions given by

$$q = \frac{1}{2\pi} \sin^{-1}\left(\frac{J - Z}{A}\right) \tag{2}$$

where J is the intensity at the end point in CPS. Then the actual distance is given by multiplying the total (non-integral) number of fringes by the lattice spacing. This measure of displacement is independent of coil voltage and interferometer spring constant calibrations, but does depend on this being linear so that the sampling points are equidistant. For example, analysis of the section in figure 7 shows 2.5 fringes between the zero crossings to either side with fractions -0.102 at the start and -0.132 at the end. The total distance is then 2.266 fringes, corresponding to 0.711 nm displacement. Talystep readings show a uniform change of 0.42 nm, a drift of 0.29 nm caused by calibration error and, particularly, temperature change during the 5 min run.

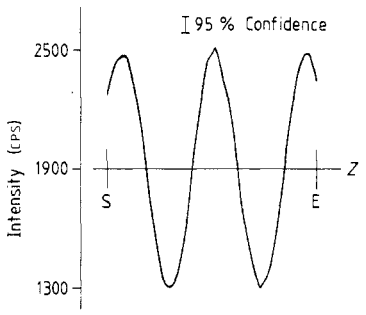

Figure 7. Example of accurate determination of distance of travel.

Displacements of less than one fringe period may be estimated using a sine curve fitting program, for which, however, a prior knowledge of the approximate parameters is required. Large displacements may be measured by performing a single step corresponding to a large number of fringes (as long as any variation in spring constant of the interferometer is known over the required range), then recording and analysing the final few fringes. Alternatively, the number of sampling points per fringe may be reduced in order to decrease the time for counting a large number of fringes, but again the final few fringes require more sampling points to enable the displacement to be measured accurately.

3.2. Precision and errors

In an instrument designed for metrological calibration it is of prime importance to estimate the precision and errors. Here the principal error sources will be computational approximation, statistical noise in intensity counting, generator and control circuit instability and thermal drift. The interaction of these through a sequence of non-linear relationships between parameters and measurands requires analysis of considerable complexity and the adoption of assumptions which are plausible but not, demonstrably, the only possible ones (Chetwynd and Schwarzenberger 1988). The analysis is summarised in some detail below, using conservative approximations to obtain error estimates which are a little high for most practical situations but not extreme for all possible situations. This leads also to a useful prediction for the optimum strategy for data collection when given overall time and range requirements.

3.2.1. Thermal and other drift. All circuits, and the lattice parameter of silicon itself, show some thermal drift. Hence, temperature stability over the period of the measurement is a necessity. The expansion coefficient of Si is $2.56 \times 10^{-6}\ K^{-1}$, therefore stability to about 0.1 K is a condition of the experiments, and electronic circuits will normally show high stability under such conditions.

Experience has shown us that the transducer under test is likely to be far more sensitive to thermal drift when

at these high sensitivities than is the x-ray interferometer and its drive. This can be used to assess transducer stability by cycling the position repeatedly over, say, a few nanometres; the calibration and drift errors in the transducer can then be evaluated separately.

X-ray photon emission closely follows a Poisson distribution. Provided that the total count, Jt, in a measurement of duration t does not become too small, the Normal approximation may be used, based on a variance numerically equal to Jt. It is thus expressed as an intensity squared

$$\sigma^2(J) = J/t. \tag{3}$$

The statistical precision can therefore *always* be improved by counting for longer at each point.

The statistical error will propograte into the error in estimating total displacement both directly through end fraction estimation, equation (2), and indirectly through the use of equation (1) in deriving the parameters of equation (2).

3.2.2. Error in the use of the Stirling algorithm. The Stirling algorithm is important for rapid data interpolation, but it is inherently an approximation. Even if the three values of intensity which it uses were known without error, the peak amplitude would be underestimated by an amount depending on the distance of the central measurement from the true peak position. Referring for notation to figure 8 for samples Δ apart with the central one φ from the peak, the readings should be

$$J_1 = Z + A\cos(\varphi - \Delta) \tag{4}$$

$$J_2 = Z + A\cos\varphi \tag{5}$$

$$J_3 = Z + A\cos(\varphi + \Delta). \tag{6}$$

Substituting these values into equation (1) and using equation (5) to eliminate the unknown A, the Stirling approximation to the peak value, $Z + A$, is expressed only in terms of J_2

$$\delta = J_m - (Z + A)$$

$$= (J_2 - Z)\left(1 - \frac{1}{\cos\varphi} + \frac{\sin^2\Delta\tan^2\varphi}{4(1-\cos\Delta)}\right). \tag{7}$$

It is readily shown that δ is always negative at a peak and positive at a trough; the amplitude is consistently underestimated. When $\varphi = 0$, there is no error, otherwise the error depends upon the sampling period to which Δ and the range of φ are related. In a typical case we take $J_m = 2000$ CPS with 24 sampling points per fringe, so the worst case $\varphi_{max} = \pi/12$. Using every third point in the Stirling algorithm, $\Delta = \pi/4$ and then $\delta_{max} = 0.005\,J_m$.

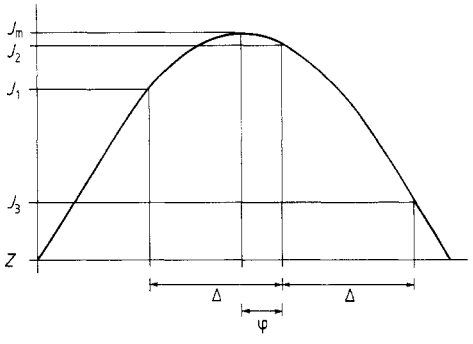

Figure 8. Notation of points for the data analysis algorithms.

Note that for planning experimental schemes based on estimated mean intensities and contrast, C, the alternative form of equation (7) would be used with CZ replacing $(J_2 - Z)$, other terms unaltered.

The algorithmic scheme can conveniently be arranged to take J_2 as the first point after the detection of a peak or trough. For an isolated feature, it is then expected that φ will be uniformly distributed in the range 0 to φ_{max} and

$$\varphi_{max} = 2\pi/f \tag{8}$$

where there are f sampling points per fringe. For reasonably small φ, δ follows φ^2 and so the standard statistics of a parabolic distribution are used to simplify equation (7) in the later analysis. Substituting equation (8) into equation (7) gives a value for δ_{max} and then

$$E(\delta) = \delta_{max}/3 \tag{9}$$

$$\sigma^2(\delta) = \tfrac{4}{45}\delta^2_{max}. \tag{10}$$

Under the proposed sampling scheme the estimate is biased with an expected value one third of its worst case. Other schemes can reduce the magnitude of, though not eliminate, the bias at the cost of additional computing to iterate around the feature.

A second error in the Stirling algorithm comes from the statistical uncertainty of the measurements J_i. This is treated under the conventional technique for functions of several variables with normally distributed errors

$$\sigma^2(F(y_1 \ldots y_n)) = \sum_{i=1}^{n}\left(\frac{\partial F}{\partial y_i}\right)^2\sigma^2(y_i). \tag{11}$$

Performing the partial derivatives directly on equation (1) shows that all three of them are simple quadratic functions of $\tan\varphi\sin\Delta/(1-\cos\Delta)$ and that those for the outer points show symmetry and partly cancel. It would be rare for the expression to exceed, or approach, unity, so approximations are introduced. It is assumed that all three measurements have a common variance, that of J_2, so that simple summation of the squared partial derivatives can be obtained. Then squared and higher order terms in the expression just quoted are neglected. This leads to the conclusion that for planning and error-bound estimation we may use the simple approximation

$$\sigma^2(J_m) \approx \sigma^2(J_2) = J_2/t \tag{12}$$

for errors derived from photon counting. The approximation will generally be conservative but does not represent a firm upper bound. Denoting equation (10) as the variance due to spatial effects and equation (12) as the variance due to temporal effects, we observe that they are independent error sources and so take the overall variance of a peak estimate from the Stirling algorithm to be their sum.

3.2.3. Error in the end-fraction estimate. The parameters A and Z used in equation (2) will each have errors of the type described in § 3.2.2 as they are computed from peak and trough values. The temporal error at each extremum may be taken as independent. However, in practice, the sampling scheme is likely to take a nominally integer value for f and so the value of φ at adjacent extrema will be highly correlated. In consequence, the spatial errors will be correlated. As it gives the most conservative result, perfect correlation will be assumed. The instantaneous spatial errors will then be equal in magnitude but opposite in direction at peaks and troughs. They will cancel in estimating Z and add in estimating A. So Z will be unbiased and A will have a bias of $-\delta_{max}/3$. Again using equation (11) to combine temporal terms the variances are then

$$\sigma^2(A) = \tfrac{1}{4}(\sigma^2(J_{max}) + \sigma^2(J_{min})) + \tfrac{4}{45}\delta^2_{max} \qquad (13)$$

while $\sigma^2(Z)$ has only the first, temporal, term.

Applying now standard methods to equation (2) leads to difficulties, for the theoretical error can go to infinity as the end fraction approaches 0.25. Hence we first use equation (11) on

$$x = \frac{J - Z}{A}. \qquad (14)$$

This can be evaluated directly from equations cited here but we note that the linear approximations in the error analysis have been compounded several times and so the analysis is only reliable for fairly low contrast. As low contrast is to be expected in practical systems, it can be further exploited by taking the sum of peak and trough variances to be twice that at the zero-crossing level. If, further, $(J - Z)^2$ is replaced by an overestimate A^2 wherever it occurs in the partial derivative coefficients of x, the simple form

$$\sigma^2(x) = \frac{1}{C^2Z^2}\left(\frac{Z(2+C)}{t} + \tfrac{4}{45}\delta^2_{max}\right) \qquad (15)$$

occurs, CZ replacing A for convenience in most real calculations. There will be bias in the estimate of x, propagated from that in A. It can be evaluated by using the forms $x + \varepsilon(x)$ and $A + \varepsilon(A)$ in equation (14) and then approximating the equation by a linear form using the binomial expansion. This gives the expected bias on x as $\delta_{max}/3CZ$ away from zero crossings.

In practice, start and end points would be expected with equal likelihood at all points of the fringe. So as estimation is always within an identified quadrant, the expected value for q would be 0.125, or 45° if expressed in phase terms. The problem of the singularity in the error analysis could be overcome by evaluating the error propagation from x to q at this point, regarding it as a 'typical error'. Given the rapid increase of error at higher values, this might lead to overly optimistic estimates compared with what could happen in reality. Therefore, we adopt the approach, but choose to perform the evaluation at the higher 60° phase point in order to increase the margin. The evaluation is simply one of substitution through equation (2) and leads to a typical error bound of

$$\sigma^2(q) = \frac{1}{C^2Z^2\pi^2}\left(\frac{Z(2+C)}{t} + \tfrac{4}{45}\delta^2_{max}\right) \qquad (16)$$

with an expected bias on q of $\delta_{max}/3CZ\pi$ away from zero.

For example, in figure 7 with 23 samples per fringe, the expected bias in the end estimates is about 0.003 fringe and the standard deviation, totally dominated by temporal effects, is about 0.025 fringe or 0.008 nm.

3.2.4. Errors in two fringe system. So far, error analysis has focused on a single fringe system as the fundamental analysis is common to all types. Providing it is noted that t refers to the counting time per channel, that is about half the time per position on a chopped beam system, the analysis remains identical up to equation (15). However, with two fringes in quadrature available, it will always be possible to evaluate the end fraction relatively close to the zero crossing level. The use of peak-level values for temporal terms may then be a little pessimistic and evaluating from equation (15) to q at a phase position of 60° is certainly pessimistic. We choose, somewhat arbitrarily, to compensate for these by evaluating instead at a phase position of 30° from zero-crossing level. The effect of this is purely a scaling of the formulae by cos 30° rather than cos 60°.

Hence, for a dual-beam interferometer, the typical worst case errors are an expected bias of $\delta_{max}/3\sqrt{3}CZ\pi$ and a variance

$$\sigma^2(q)_2 = \frac{1}{3C^2Z^2\pi^2}\left(\frac{Z(2+C)}{t} + \tfrac{4}{45}\delta^2_{max}\right). \qquad (17)$$

3.2.5. Optimising data collection strategy. While the x-ray interferometer itself is not unduly sensitive to temperature (or other mechanical disturbances), it is known that the transducers to be calibrated or tested on it often have poor thermal performance at the sub-nanometre level. It will often therefore be desirable to complete a test in the shortest time consistent with the achievement of the required precision. Alternatively, we may wish to obtain the most possible precision from a test which is restricted, externally, to some maximum total time.

In general, as the previous analysis shows, accuracy in fringe analysis is improved by both increasing the counting time per point and increasing the number of points per fringe. These are inconsistent with an overall time constraint since both imply that accuracy improves continuously with measurement time. The strategy for best compromise is not obvious, particularly as practical systems will have time overheads such as a settling period after movement of the phase chopper.

The general nature of the error behaviour is illustrated by figure 9, an isometric plot of the error as a function of t and f, the time per point and the number of points per fringe. It is essentially a plot of equation (16) with the parameters $C = 0.25$, $Z = 3000$, $\Delta = \varphi$. Note that the t axis is logarithmic. It can be seen that there is a valley in the plot so that a best combination of t and f is predictable. However, once t and f become reasonably

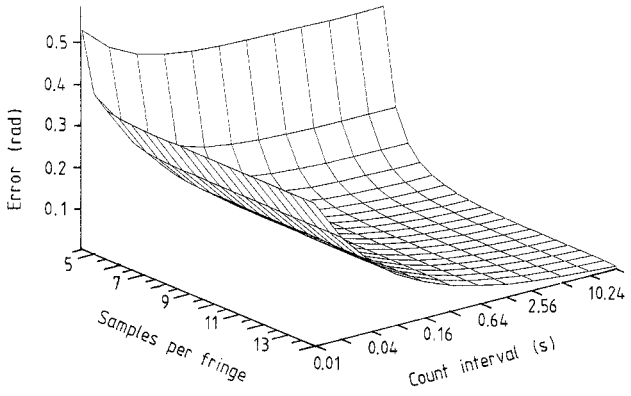

Figure 9. View of statistical and interpolation errors as function of number of points per fringe (f) and counting time per point (t).

large, the rate of change of error with either variable is slight. Above, say, $t = 2$ s and $f = 7$ there is considerable freedom of choice without serious disadvantage arising.

To choose a point in this relatively flat plane, we use the strategy of matching errors from different sources. This is based on the observation, for example, that reducing the spatial errors will have negligible effect if the temporal errors are already the larger component. The systematic bias is difficult to handle statistically and is anyway closely related in magnitude to that of the spatially derived variance. Thus the strategy is to equalise the spatial and temporal terms of equation (16) namely

$$\frac{Z(2+C)}{t} = \tfrac{4}{45}\delta_{\max}^2 \tag{18}$$

where $\delta_{\max}$ is a function of f.

To scale a total distance D in total time T implies that the time per position will be Td/Df, where d is the relevant lattice spacing. We expect an overhead time at each position, τ, so for a single fringe system

$$t_1 = \frac{Td}{Df} - \tau. \tag{19}$$

For a dual-beam chopped system, the counting time will be half the available time at each position and the settling time will apply to each counting period. This gives

$$t_2 = \frac{Td}{2Df} - \tau. \tag{20}$$

Thus, substituting $\varphi = 2\pi/f$ in equation (7), using CZ in place of $(J_2 - Z)$, to obtain $\delta_{\max}$ and substituting that value and the appropriate one of equations (19) or (20) into equation (18) gives a non-linear equation for f. This can be readily and rapidly solved on a small computer by iterative methods. Using a commercial package on an Olivetti M24 with floating point accelerator it takes, typically, 2–3 s to evaluate. The solutions show that for most sensible combinations for distance and time, the best strategy is to use a small number of samples, often as few as six per fringe, and spend plenty of time counting. This reflects the contrast and relatively low intensities quoted in the examples. It does not generate easy-to-visualise fringes for plotting purposes and so larger numbers of samples than ought to be the case have been used in the examples in this paper.

The final point of experimental selection is the user-selectable relationship between Δ and φ in the Stirling algorithm. Δ must be a multiple of φ and should not exceed $\pi/2$ for use in the algorithm. From equation (7), it is seen that Δ influences the spatial error through the factor $\sin^2\Delta/(1-\cos\Delta)$ in one term only. This factor has unity value at $\Delta = \pi/2$ and rises steadily as Δ reduces to 2 at $\Delta = 5°$. When $\varphi_{\max}$ is very large, it is clearly appropriate to reduce the influence of the $\tan^2\varphi$ term by choosing Δ near to $\pi/2$. At small $\varphi_{\max}$ the relative growth rates of the second and third terms of equation (7) make the overall error lower if a smaller Δ is selected. The effect is slight and making Δ variable may be an unnecessary complication in the analysis process. If desired, an iterative optimisation for the selected $\varphi_{\max}$ can be executed.

4. Talystep evaluation

To illustrate the practicality and sensitivity of x-ray interferometer calibrators we report some of our work with the Rank Taylor Hobson Talystep head. This was chosen as it was known to be one of the most sensitive commercial systems available. Whitehouse (1975), reported evidence that it could resolve to the dimensions of crystal lattice spacings and modern electronics gives higher sensitivity than was then available. The results presented here have demonstrated that confidence in its abilities was quite justified. The inductive gauge is certainly capable of responding to a displacement of around 10 pm, see the response to the turnover in figure 5. This limit relates to the particular computer-interface electronics used in these experiments. It may not represent the ultimate capability of the transducer. However, the effects of both electrical and mechanical noise at the transducer start to dominate, being commonly above 100 pm RMS in a 25 Hz bandwidth (Bowen *et al* 1985, Chetwynd 1987). Thus this discrimination is a realistic, practical limit for configurations which allow the Talystep to be used for its intended purpose and is quite adequate for that purpose.

When driven by a smoothly changing ramp, rising by 10 nm in approximately 90 min and confirmed by the fringe count, Talystep also showed a linear increase but of about 18 nm amplitude. This value will be influenced by both calibration errors and thermal drifting so the divergence is not particularly remarkable: on the basis of the discussion below, the whole of the 8 nm divergence could be attributable to a linear temperature drift of 0.02 K. This very slow ramp provides a severe test for the system. However, superimposed on the ramp is an oscillatory error of about 1 nm amplitude with a period of about 15 min. The period is rather variable but does not correlate obviously with either temperature cycling in the room or with the rate of ramp of the Talystep. Its cause is unknown, but it may be a manifestation of the behaviour reported by Chetwynd *et al* (1983), although

their estimate in terms of a rate would imply a larger amplitude than we detect.

While the sensitivity and noise characteristics of the Talystep transducer are extremely good, its thermal sensitivity is more problematic. Temperatures were variously monitored around the experimental system, mainly by the use of bead thermistors. These were used as the time-constant determining resistor in an oscillator circuit which allows high sensitivity without difficulties arising from the use of long leads for remote monitoring. These were calibrated directly against the open-circuit voltage of a type-K thermocouple giving values of around 200 Hz K^{-1} at close to 20 °C. As temperature change is being measured, the lack of a close absolute calibration does not matter. On the basis of sampling every 5 or 10 s a change of 1 mK is detectable. The devices are non-linear but over the small changes being measured here they may be treated as linear within the overall estimated accuracy of 5% for the measurements. Absolute temperature was monitored and cross checked by a class B platinum resistance thermometer and a precision mercury-in-glass thermometer to 0.1 °C.

The typical thermal performance, at 20 °C nominal, is shown in figure 10. Here the system has been monitored over approximately 60 h while the temperature control on the room is relaxed so that it follows the diurnal cycles of the overall building. In this way, the system will be almost in thermal equilibrium with its environment at all times and geometric distortions due to temperature gradients will be minimised. The net effect of expansion within the Talystep measuring loop while the interferometer is in its equilibrium position is around 400 nm K^{-1}. It is not possible with certainty to separate the contributions of different parts of the loop, but it is clear that the Talystep is the main contributor. The transducer cannot be constructed from just one material and so several with different coefficients of expansion are used in order to get a degree of compensation around its measurement path. It is known that some of the materials used in Talystep were changed, for practical reasons, some years ago and this has increased its temperature sensitivity. One of the earlier type of head (approximately 1970 construction) was also tested, using, as closely as could be achieved, the same conditions. A similar overall pattern of behaviour was discerned but with a sensitivity

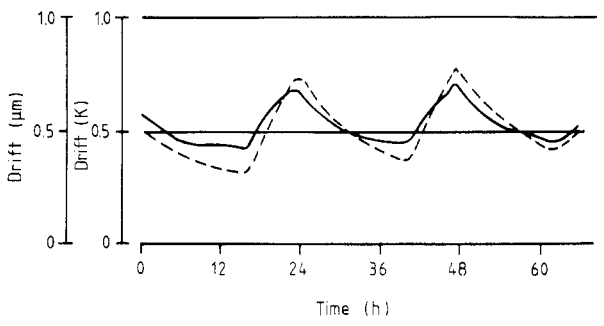

Figure 10. Temperature drift of the system with environmental temperature control switched off. Full curve: thermistor output; broken curve: Talystep output.

reduced to around 50 nm K^{-1}. With the usual head, temperature control to the order of 1 mK is needed to obtain the full performance from the instrument. In fact, this is not as severe a constraint as it might seem, for this need be held only for the duration of a particular measurement, typically a few minutes. Given reasonable care over conditions, the thermal inertia of the system provides this once equilibrium conditions are achieved. In this context we note that the time to reach equilibrium can be much longer than may commonly be supposed. The use of aluminium for these devices has been justified by exploiting its high conductivity to minimise thermal gradients. In tests such as those of figure 10, probes placed in the measurement loop immediately above the monolith and on the main body of the transducer (a physical separation of around 50 mm) showed the same cyclic patterns but with a phase delay of up to two hours between them. The practicalities of routine work to extreme precision thus seem better served by a minimum-expansion rather than a minimum-gradient philosophy. The evidence from this work confirms that the Talystep-like configuration made from ultra-low expansion materials used in the National Physical Laboratory 'Nanosurf' (Lindsey *et al* 1988) will give close to ultimate performance.

Both Talystep heads were also examined for linearity by measuring their response to a shift of 0.98 nm at points in their range ± 2 μm, ± 1 μm and 0 μm relative to the null point of the transducer with the electronic 'pen shift' being used to back-off the signal. A scatter of mean values over $\pm 5\%$ of nominal step was found but this is of the order of the standard deviation of the measurements and cannot be regarded as significant, particularly as no systematic trend was observable. The small-step gain of the transducer maintains value across the whole working range of the transducer.

5. A portable system

Following the success of the calibration system on the large test-bed, a second system was built to demonstrate the practicality of the technique within a normal calibration room. In essence the design criteria were for a desk-sized system, completely radiation shielded, having very easy access for the placement and removal of the transducers that are to be calibrated.

The basic x-ray optical layout of source, collimator, monolith, beam chopper and detector were the same as the system already described. However, a Kevex miniature x-ray tube of 60 W maximum power (60 kV, 1 mA) is used in place of the larger source. A water-cooled Mo K_α tube is used to give maximum temperature stability in the system. The output is stable to better than 0.2% relative standard deviation over a 4 h period and the temperature stabilises a few degrees above ambient after 1 h. The whole optical system is enclosed within a sheet steel box having dimensions approximately 1300 × 500 × 300 mm. The gauge mounting is external to this box. Details of the gauge and monolith mounts, shown schematically in figure 11, are the only significant changes other than the

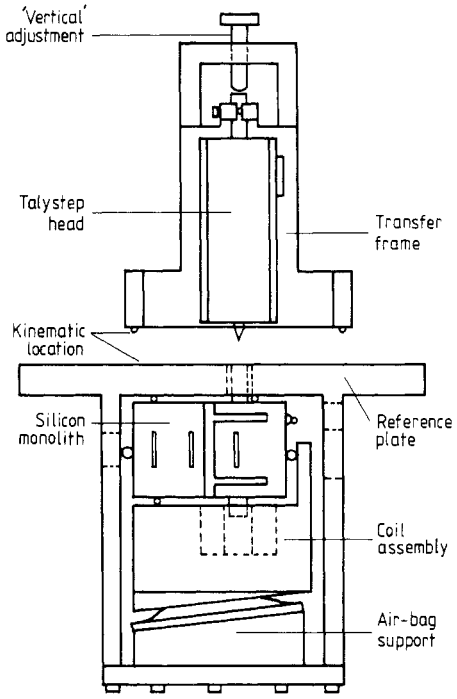

Figure 11. Mounting of interferometer in portable system.

different source. The transducer is mounted on a standardised frame which mounts kinematically on the top surface of the reference plate held by gravity. The mounting details can be readily changed for different applications. In our tests, the Talystep head was held on a friction grip similar to that used in the Nanosurf instrument. Setting to position was by a micrometer pusher which was backed off during measurements. Details of the kinematic mounts of the monolith and coil carrier to the reference plate are different between the systems but the principle remains the same. The use of the angled plate and air bag provides a force closure system approximating more closely to a body force than does the earlier spring system. This is because the inherently low shear strength of the bag prevents the friction of the contact from injecting significant lateral forces into the mounts. The plate is angled to supply a force component on the side wall of the monolith which is used as a reference point. The air bag is made from standard bicycle inner-tube components.

The major difference in performance between the two systems is simply the result of having less than one twentieth of the x-ray power in the portable one. Thus to achieve the same counting statistics, longer periods are required (though not 20 times longer since the tube is more efficient). Usually it is preferred to keep the overall measuring time relatively short so as to reduce the requirements for temperature control and, in consequence, to accept poorer definition in the fringes. The intensity of the 3 mm × 1 mm beam after diffraction is typically up to about 1000 CPS. With the chopper in place, each half-beam has a maximum of 400–500 CPS so the statistical error will not be too great even for short counting times.

Figure 12 shows the fringe display with a sampling

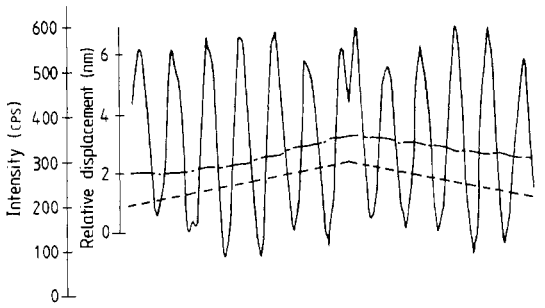

Figure 12. Results from portable interferometer system. Demand signal varies uniformly with time and total duration is about 300 s. ---- Coil demand; —·—·— Talystep output; —— x-ray intensity.

frequency of eight points per fringe, 3 s counting time for each intensity measurement and contrast of about 0.2. The standard deviation of the end-fraction of a fringe is then estimated at 0.013 nm, largely due to counting statistics. The bias in the estimation is less than 0.005 nm. Thus, overall, the error in distance measurement will be within about ± 0.02 nm at 68% confidence. This is perfectly adequate for the great majority of applications. The portable system is now installed at the National Physical Laboratory.

6. Conclusions

The techniques and results presented show that x-ray interferometry is a practical method of calibrating micro-displacement transducers at the sub-nanometre levels, for which there are no alternative techniques. The performance of the larger system proves that a highly traceable calibration to considerably better than 10 pm can be achieved if desired, although improvements beyond 10 pm may not be warranted by the transducers. Moreover the successful demonstration of the portable calibrator based on a miniature x-ray source shows that this technique is available to any Standards Room of good quality.

Work is currently proceeding on the development of more generally applicable devices based on the principles used here. In particular, developments in the design of the monolith and the metrological loops and in the data analysis, for example through phase measurement interferometry, should yield a system which is simultaneously of somewhat higher performance, cheaper to construct and more convenient to use.

Acknowledgments

This work has been generously supported by NPL grant number RD163/04 and latterly by SERC grant GRD/95845. We gratefully acknowledge the enthusiastic support of Professor A Franks and his colleagues at the National Physical Laboratory. We thank also for their help and comments Professor M Hart FRS and in the Microengineering Centre Mrs H J Brennan, Mr D Robinson, Mr C Fountain and Dr S T Davies.

References

Becker P, Seyfried P and Siegart H 1982 The lattice parameter of highly pure silicon single crystals. *Z. Phys.* B **48** 17–21

Bonse U and Hart M 1965 An x-ray interferometer *Appl. Phys. Lett.* **6** 155–6

Bowen D K, Chetwynd D G and Davies S T 1985 Calibration of surface roughness transducers at angstrom levels using x-ray interferometry *Proc. S.P.I.E.* **563** 412–9

Chetwynd D G 1987 Vibration control in sub-nanometre metrology *Proc. SPIE* **732** 47–57

Chetwynd D G and Schwarzenberger D R 1988 Accuracy estimation for fringe division in x-ray interferometry *Microengineering Report ME70* University of Warwick

Chetwynd D G, Siddons D P and Bowen D K 1983 X-ray interferometer calibration of microdisplacement transducers *J. Phys. E: Sci. Instrum.* **16** 871–4

Creath K 1988 Phase-measurement interferometry techniques *Progress in Optics XXVI* ed. E Wolfe (Amsterdam: North Holland) pp 349–93

Deslattes R D and Henins A 1973 X-ray to visible wavelength ratios *Phys. Rev. Lett.* **31** 972–5

Franks A 1984 X-ray optics – a challenge to precision engineering *Proc. Int. Symp. for Quality Control in Production* (Tokyo: Japanese Soc. Prec. Eng.) pp 8–17

Hart M 1968 An Angstrom ruler *J. Phys. D: Appl. Phys.* **1** 1405–8

—— 1975 Review Lecture: Ten years of x-ray interferometry *Proc. R. Soc.* A **346** 1–22

Lindsey K, Smith S T and Robbie C J 1988 Sub-nanometre surface texture and profile measurement with 'Nanosurf 2' *Annals CIRP* **37** 519–22

Rodriguez A R D and Siddons D P 1979 Inexpensive computer-controlled experimentation *J. Phys. E: Sci. Instrum.* **12** 403–8

Schwarzenberger D R, Chetwynd D G and Bowen D K 1989 Phase measurement x-ray interferometry *X-ray Sci. Technol.* at press

Smith S T, Chetwynd D G and Bowen D K 1987 The design and assessment of monolithic spring systems *J. Phys. E: Sci. Instrum.* **20** 977–83

Whitehouse D J 1975 Some ultimate limits on the measurement of surfaces using stylus techniques *Meas. Control* **8** 147–51

Whitehouse D J, Bowen D K, Chetwynd D G and Davies S T 1988 Nano-calibration for stylus-based surface measurement *J. Phys. E: Sci. Instrum.* **21** 46–51